Chemical Science

ROYAL SOCIETY OF CHEMISTRY

EDGE ARTICLE

View Article Online
View Journal | View Issue

Cite this: *Chem. Sci.*, 2025, **16**, 21121

All publication charges for this article have been paid for by the Royal Society of Chemistry

Nonlinear current stimulation unlocks high-performance Zn–Mn batteries *via* reversible phase transformation

Yang Song,[a] Haidong Zhong,[a] Tingting Hu,[a] Jun Du,[a] Changyuan Tao*[ab] and Qian Zhang*[a]

The intrinsic complexity of reactions in Zn–Mn batteries constrains their practical deployment, necessitating precise control over dissolution and deposition processes. Here, we employ a stepwise evolution of current signals—from steady-state constant current through symmetric and asymmetric sine waves to chaotic regimes—to systematically investigate the coupling between nonlinear electrical signals and electrode reactions. Remarkably, chaotic currents enhance the reversible transformation between $Zn_4SO_4(OH)_6{\cdot}nH_2O$ (ZSH) and $Zn_xMnO(OH)_2$ (ZMO), revealing for the first time a direct correlation between waveform nonlinearity and electrochemical modulation. This ZSH/ZMO interconversion, alongside Zn^{2+}/H^+ insertion and extraction, underpins the cathodic reaction mechanism. Accumulation of inactive ZSH/ZMO phases emerges as the primary factor driving kinetic decay. Following seven cycles of chaotic activation, Zn–Mn batteries exhibit improved capacity, rate performance and cycling stability. The approach translates to flexible cells, delivering 92.23 mAh g^{-1} with 76.37% retention after 1550 cycles at 1 A g^{-1}. *In situ* visualization, SEM imaging, and comprehensive thermodynamic and dynamic analyses reveal that nonlinear current stimulation reconstructs fractal mass transport pathways within the electrode, thereby optimizing ion pathways and structural stability. This study bridges nonlinear circuit dynamics and Zn–Mn electrochemistry, presenting a promising strategy to high-performance aqueous Zn–Mn batteries.

Received 12th August 2025
Accepted 4th October 2025

DOI: 10.1039/d5sc06137g

rsc.li/chemical-science

Introduction

Rechargeable aqueous zinc-ion batteries (AZIBs) are promising candidates for large-scale renewable energy storage, owing to their intrinsic safety and the abundant availability of zinc in the Earth's crust.[1–5] Among various systems, zinc–manganese batteries have attracted significant attention due to their environmental friendliness, non-toxicity, and relatively high output voltage. Manganese dioxide (MnO_2), a low-toxicity and cost-effective cathode material, typically has spinel, tunnel, or layered structures, with its basic structural unit consisting of edge- or corner-sharing MnO_6 octahedra.[6–8] MnO_2 exhibits a single-electron transfer capacity of approximately 308 mAh g^{-1} and a theoretical two-electron transfer capacity of about 616 mAh g^{-1}, demonstrating high energy storage potential.[9–11] However, its poor electronic conductivity and limited cycling stability in aqueous Zn‖MnO_2 batteries remain significant challenges that hinder further development.

The energy storage mechanism of aqueous Zn–Mn batteries involves a synergistic interplay of Zn^{2+} intercalation/deintercalation, MnO_2 redox reactions, and Mn^{2+}-induced conversion processes.[12–14] During discharge, Zn^{2+} ions are released from the anode, migrate through the electrolyte, and partially intercalate into the MnO_2 lattice or participate in the formation of intermediate phases such as Zn_xMnO_2 and MnOOH, accompanied by the reduction of Mn^{4+} to Mn^{3+}/Mn^{2+}. In acidic environments, Mn^{2+} tends to dissolve into the electrolyte, leading to active material loss. Additionally, Mn^{2+} reacts with Zn^{2+}, SO_4^{2-}, and OH^- ions to form precipitation products like $Zn_4SO_4(OH)_6{\cdot}xH_2O$ (ZSH), which are quasi-reversible or irreversible and can impair electrode stability.[15,16] Upon charging, some of the ZSH deposits are re-oxidized into ZMO-type phases or redissolved into the electrolyte, forming a dynamic cycle of deposition–dissolution–conversion. Thus, the energy storage behavior of this system is governed by a multi-mechanism coupling of ion intercalation, redox transformation, and conversion precipitation.[17–19] Ongoing research has highlighted the important role of the $Zn_4SO_4(OH)_6{\cdot}xH_2O$ (ZSH) conversion reaction in the electrochemical behavior of MnO_2 cathodes. Chen *et al.* demonstrated that the reversibility of the conversion reaction between ZSH and $Zn_xMnO(OH)_2$ (ZMO) is a key factor in the cycling stability of sulfate-based

[a]*School of Chemistry and Chemical Engineering, Chongqing University, Chongqing 400044, China. E-mail: qianz@cqu.edu.cn*

[b]*State Key Laboratory of Coal Mine Disaster Dynamics and Control, Chongqing University, Chongqing, 400044, China*

aqueous Zn–Mn batteries.[20] Additionally, some studies have shown that excessive accumulation of ZSH on the MnO_2 cathode surface significantly contributes to the deterioration of electrochemical performance. To address this challenge, strategies to regulate and improve the deposition behavior of ZSH have emerged as effective means to enhance the performance of rechargeable aqueous Zn–MnO_2 batteries. For example, Jiang *et al.* regulated MnO_2 *via* a DIMS (deep ion mass transfer) strategy to suppress its affinity toward OH^- and SO_4^{2-} ions, thereby effectively preventing the formation of the ZSH passivation layer. It is worth noting that the conversion reaction between ZSH and ZMO nanosheets is highly sensitive to voltage, and the upper cut-off voltage during charging significantly influences the reversibility of this transformation.[21] Wang *et al.* observed that during long-term cycling, the MnO_2 cathode tends to be passivated by electrochemically inactive ZMO, which exhibits poor reversibility, low electronic and ionic conductivity, and leads to degraded rate capability and capacity fading. In contrast, when the cut-off voltage exceeds 1.85 V, the conversion reaction is activated, promoting the formation of highly reversible and electrochemically active ZMO while sustaining stable capacity output and suppressing the accumulation of inactive species.[22] Therefore, the reversible transformation between ZSH and ZMO is of great significance for improving cycling stability.

According to chemical kinetics theory, reaction rates exhibit nonlinear dependence on variables such as reactant concentration, electrode potential, and temperature. Such nonlinearity can lead to multistability, oscillations, self-organization, or even chaotic behavior, especially in systems with feedback mechanisms or coupled mass transport processes.[23–27] In Zn–Mn batteries, these nonlinear dynamics primarily manifest in the coupling between electrode reactions and ion transport. The multi-electron conversion of MnO_2 involves multiple oxidation states of manganese ($Mn^{4+} \rightarrow Mn^{3+} \rightarrow Mn^{2+}$), with each step characterized by distinct, nonlinear reaction kinetics that influence the overall electrochemical performance.[28–33] Moreover, processes such as phase transitions, dissolution–reprecipitation, and other complex behaviors further enhance these nonlinear effects.[32,34–36] The reaction pathways and kinetic processes are highly sensitive to the form and magnitude of external current or voltage perturbations, meaning that current fluctuations from the power source can not only alter reaction rates but may also shift the reaction mechanisms themselves.[37–40] Understanding and controlling these nonlinear processes is crucial for improving the cycling stability and rate capability of Zn–Mn batteries.

Results and discussion

To systematically evaluate the influence of voltage and current perturbations on battery charging performance, a series of stepwise excitation experiments were designed (Fig. 1a). Specifically, five types of dynamic current-pulse (Fig. S1), constant-voltage charging (Fig. S2), single-frequency sine wave (Fig. S3), non-uniform amplitude sine wave (Fig. S4), and chaotic nonlinear circuit (NC) (Fig. 1b, c and S5, S6) – were applied to the Zn||a-MnO_2/Ti_3C_2F cell for short-term charging (15 min), followed by discharge at a constant current density of 200 mA g^{-1}. Detailed descriptions of the power supply parameters are provided in the SI. The results (Fig. S7) reveal a pronounced enhancement in electrochemical response, with increased energy storage capacity as the excitation evolved from ordered to chaotic forms. This trend highlights the crucial role of dynamic current regulation, particularly chaotic excitation, in activating electrode reactions.

To establish an efficient activation protocol based on chaotic current, complete activation is defined by the emergence of negative current fluctuations near full voltage, accompanied by a positive current density below 50 mA g^{-1}. This ensures that the observed electrochemical responses arise from intrinsic ion transport and reaction processes rather than transient surface charge accumulation, enabling full activation of the system. As shown in Fig. 1d–f, a systematic evaluation of activation performance under different charge–discharge cycles determined that seven cycles represent the optimal activation conditions. Notably, the mA–*t* curve and its FFT and PSD analyses (Fig. S8) demonstrate that chaotic current exhibits dominant low-frequency intensity while retaining continuous contributions across higher frequencies, indicative of a broadband feature. This broadband nature implies that chaotic current operates simultaneously on multiple timescales. As a result, it continuously mitigates concentration polarization, suppresses byproduct accumulation, and enhances electrode kinetics and cycling stability. As shown in Fig. 1g and h, the oxidation peaks primarily correspond to H^+/Zn^{2+} intercalation processes, while the reduction peaks are associated with the formation of ZSH. With continued cycling, the reversible ZSH conversion stabilizes, giving rise to two distinct redox pairs corresponding to H^+/Zn^{2+} intercalation/deintercalation and the ZSH reversible transformation, respectively. Furthermore, the treated electrode exhibits a significantly reduced redox peak separation (443 mV and 248 mV), compared to the untreated sample (454 mV and 263 mV), indicating lower polarization, reduced charge-transfer resistance, and more efficient reaction kinetics.[41–43] In addition, the CV curves of the treated sample remain highly consistent over multiple cycles, with well-defined and symmetric peak shapes, suggesting a single reaction pathway, structural stability, and excellent electrochemical reversibility. In contrast, the untreated electrode displays evident peak shifts and multiple complex peaks upon repeated scanning, implying structural instability and non-ideal interfacial behavior. In summary, nonlinear treatment not only improves charge transfer kinetics but also enhances interfacial structural control and electrochemical reaction stability.

To systematically evaluate the activation effect of nonlinear current excitation on the cathode material, electrochemical impedance spectroscopy (EIS) measurements were conducted. As shown in Fig. 1i, compared with the initial state, the cells exhibited a notable decrease in interfacial charge-transfer resistance (R_{ct}) under both fully charged (NC-7–1.9 V) and fully discharged (NC-7–0.8 V) conditions, with values reduced from 155.4 Ω to 128.4 Ω. This reduction indicates that the electrode surfaces were effectively activated and the charge-

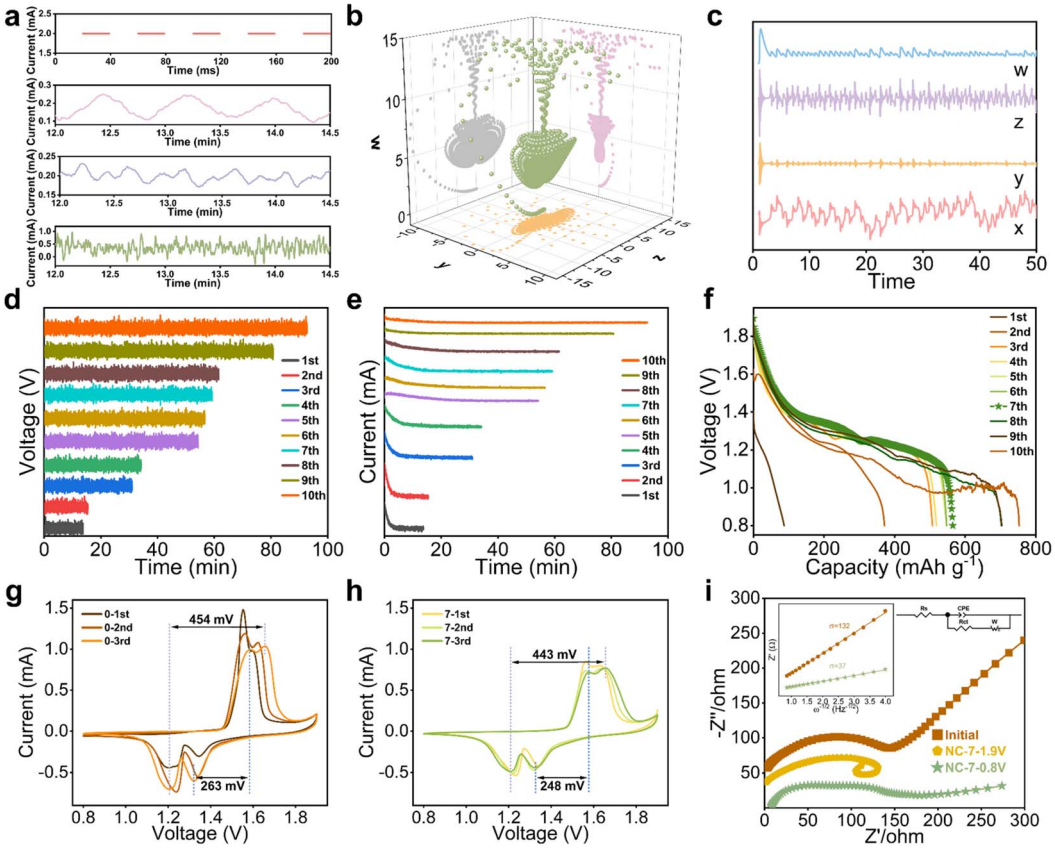

Fig. 1 (a) Current profiles collected in different charging modes; (b and c) signal waveforms generated by the system and the corresponding chaotic attractors; (d–f) current, voltage, and discharge capacity curves during chaotic activation with varying numbers of charging cycles; (g and h) comparison of CV curves before and after chaotic activation; (i) EIS spectra, Nyquist plots, and the $Z'-\omega^{-1/2}$ relationship in the low-frequency region for chaos-activated and pristine electrodes.

transfer kinetics were significantly enhanced.[44,45] At 1.9 V, the low-frequency diffusion tail in the EIS spectrum is markedly attenuated, indicating that interfacial reactions may dominate over bulk diffusion. Notably, subsequent SEM (Fig. 2j) and ToF-SIMS (Fig. 4) analyses of the cycled chaotic-activated electrode reveal no compact passivating layer, while showing extremely weak S-related signals together with a uniformly distributed Zn signal, consistent with the reversible conversion between ZSH and ZMO.[46–51] Further analysis at 0.8 V reveals a compressed charge-transfer semicircle and a distinct Warburg tail in the Nyquist plot, reflecting low interfacial resistance and unimpeded ion diffusion pathways. Compared to the initial state, the system shows markedly reduced diffusion resistance, corresponding to a higher ion diffusion coefficient ($D_1 = 7.19 \times 10^{-13}$ cm^2 s^{-1} > $D_0 = 5.65 \times 10^{-14}$ cm^2 s^{-1}). In summary, nonlinear current excitation not only effectively activates the electrode material but also induces distinct structural and kinetic advantages at both ends of the charge–discharge range, thereby achieving comprehensive performance enhancement across the full voltage window.

To investigate the effect of current perturbations on the reversible transformation between ZSH and ZMO, we developed a transparent Zn–Mn battery setup to enable direct visual observation of the conversion process. As shown in Fig. S9, ZSH was partially deposited on FTO glass *via* electrodeposition to serve as the cathode, while a 2 M $ZnSO_4$ + 0.5 M $MnSO_4$ aqueous solution was used as the electrolyte, and polished zinc foil served as the anode.[20] Different charging modes were applied within a voltage window of 0.8–1.9 V to simulate the operational transformation between ZSH and ZMO. As shown in Fig. 1a and S10, the ZSH region gradually turned brown upon charging, and then faded during discharge, eventually reverting to a lighter color at 0.8 V. However, as cycling progressed, brownish irreversible products gradually accumulated on the FTO surface, severely compromising the reaction reversibility. Notably, under chaotic circuit excitation, the formation of these irreversible species was significantly suppressed. Using image extraction and analysis techniques (Table S1), we quantitatively evaluated the coverage ratio of inactive products during each cycle, confirming that chaotic current promotes the ZSH/ZMO conversion and mitigates cathode degradation. Additionally, control experiments showed that bare FTO exhibited no electrochemical activity within the working voltage range, verifying that the observed transformations originate from ZSH/ZMO chemistry. Further XRD and optical microscopy analyses (Fig. 2b, c and S11) reveal that the as-synthesized ZSH exhibits a sharp characteristic peak at ~10.1° (PDF#44-0673 and PDF#39-0688). This peak completely disappears upon charging

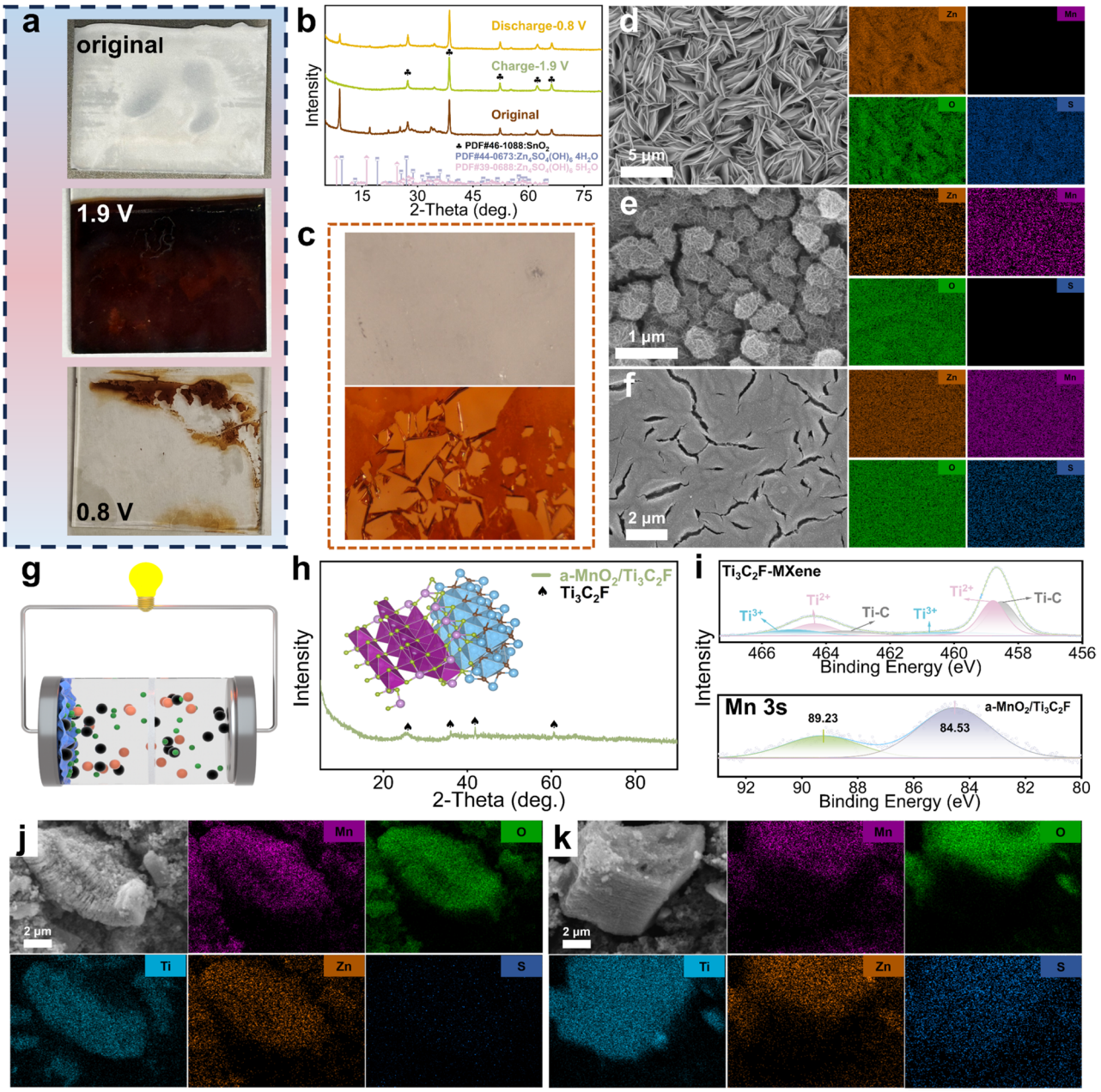

Fig. 2 The Zn-ZSH (FTO) battery system: (a–c) photographs of the FTO electrode, XRD patterns, and optical images after cycling; SEM and elemental mapping results of (d) the initial ZSH, (e) the electrode charged to 1.9 V under chaotic current, and (f) the inert products formed during cycling. The Zn-a-MnO_2/Ti_3C_2F battery system: (g and h) schematic illustration of the cathode structure and the XRD pattern; (i) XPS analysis; (j and k) SEM and elemental mapping images of the electrode after cycling at 1.9 V and 0.8 V, respectively.

but reappears with markedly reduced intensity in the brown deposits after discharge. Correlating with the electrochemical process, ZSH is predominantly present in the discharged state (0.8 V), whereas ZMO emerges in the charged state (1.9 V). SEM and elemental mapping analyses (Fig. 2d–f) further demonstrate that the initial sheet-like ZSH structures transform into nano-spherical ZMO during charging. With prolonged cycling, however, these structures progressively aggregate into inert clusters, forming a surface layer that impedes ion transport and reaction kinetics, ultimately resulting in performance degradation. In contrast, chaotic current effectively suppresses such structural deactivation and markedly enhances the reversibility of the ZSH/ZMO conversion.

We also conducted full-cell tests by using a-MnO_2/Ti_3C_2F as the cathode material to validate the applicability of this activation strategy in practical systems. This heterostructure combines the advantages of amorphous and two-dimensional layered structures, offering abundant ion diffusion pathways and mechanical buffering capability (Fig. 2g–i).[52–54] As shown in Fig. 2j and k, after 500 cycles with chaotic activation, the

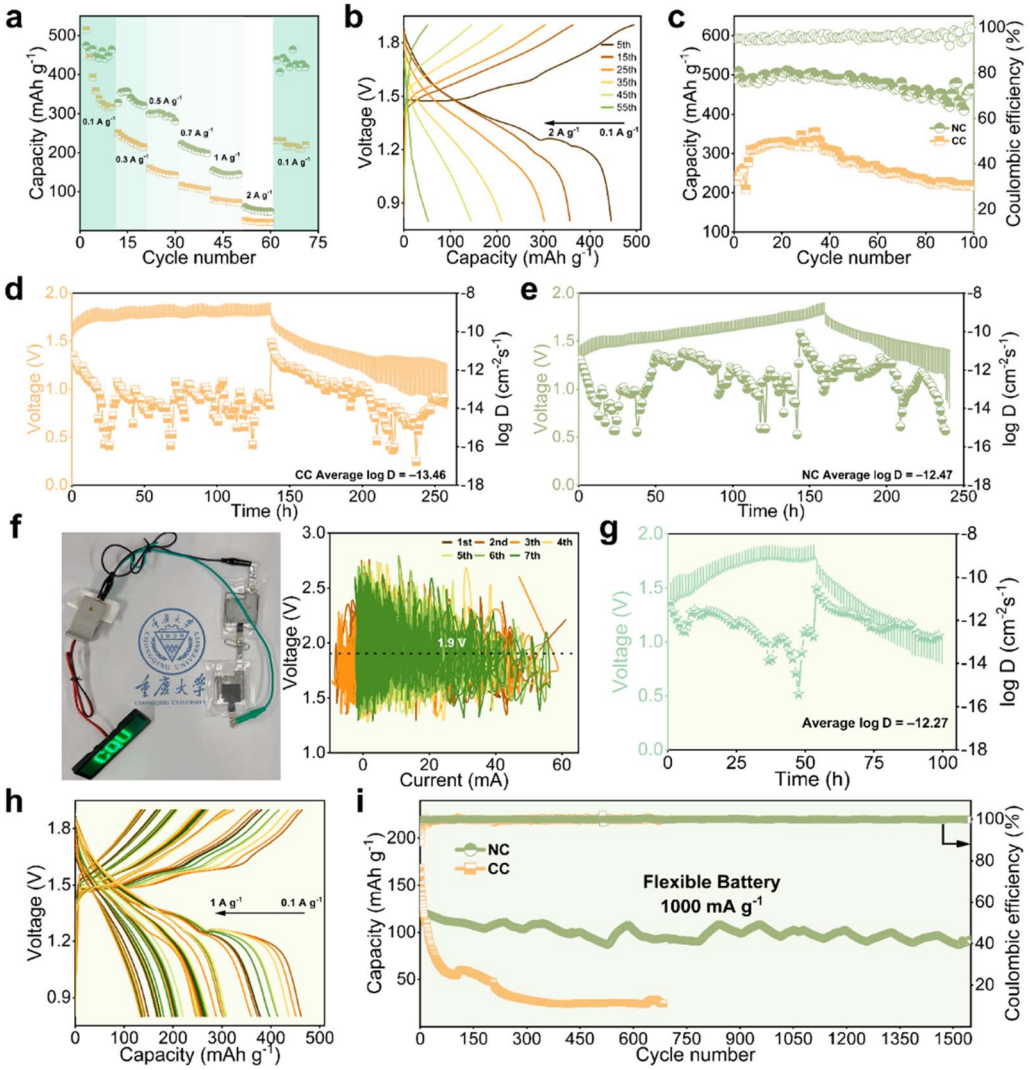

Fig. 3 (a and b) Rate performance and GCD curves at various current densities; (c) cycling performance at 200 mA g^{-1}; (d and e) GITT tests of the chaos-activated and pristine electrodes. (f) Photograph and voltage–current image of the flexible battery based on the chaos-activated electrode; (g) GITT test; (h) GCD curves at various current densities; (i) long-term cycling performance at 1000 mA g^{-1}.

cathode retained its well-defined 2D morphology, with uniformly distributed Zn and Mn elements. The surface transformation between ZSH and ZMO exhibited high spatial uniformity and reversibility, highlighting the effectiveness of this strategy in regulating structural stability and optimizing electrochemical performance.

We have demonstrated an effective strategy for electrode activation with chaotic current excitation. The following performance evaluation is focused on a systematic comparison between the activated electrode under nonlinear current (chaos-activated, NC) and those under conventional constant current conditions (original, CC) at the full-cell level. Fig. 3a illustrates the rate capabilities of the chaos-activated electrode at various current densities of 100, 300, 500, 700, 1000, and 2000 mA g^{-1}. The specific capacities (441.8, 338.2, 295.6, 208.4, 146.1 and 52.5 mAh g^{-1}) are significantly higher than those of the original electrode (290.9 mAh g^{-1}, 229.9 mAh g^{-1}, 149.1 mAh g^{-1}, 109.0 mAh g^{-1}, 75.1 mAh g^{-1}, and 22.7 mAh g^{-1}). As shown in Fig. 3b, galvanostatic charge–discharge (GCD) curves reveal that increasing current density shifts the electrochemical mechanism from diffusion-controlled to surface-controlled processes, evidenced by the merging of voltage plateaus. This suggests a diminished role for deep ion intercalation/deintercalation and highlights the importance of fast kinetics in surface phase transformations between ZSH and ZMO. Cycling performances at 200 mA g^{-1} (Fig. 3c) show that chaos-activated electrode retains a reversible capacity of 430.3 mAh g^{-1} after 100 cycles, compared to only 291.9 mAh g^{-1} for the original electrode. Furthermore, to verify the universality of chaotic activation, additional tests were performed on four commercial MnO_2 polymorphs (α, β, γ, and δ) (Fig. S12), which also demonstrated effectiveness. The Galvanostatic Intermittent Titration Technique (GITT) was employed to determine the diffusion coefficients during charge–discharge at a current density of 100 mA g^{-1}. As shown in Fig. 3d and e, the chaos-activated cathode exhibits a higher average $\log D$ value of −12.47 compared to

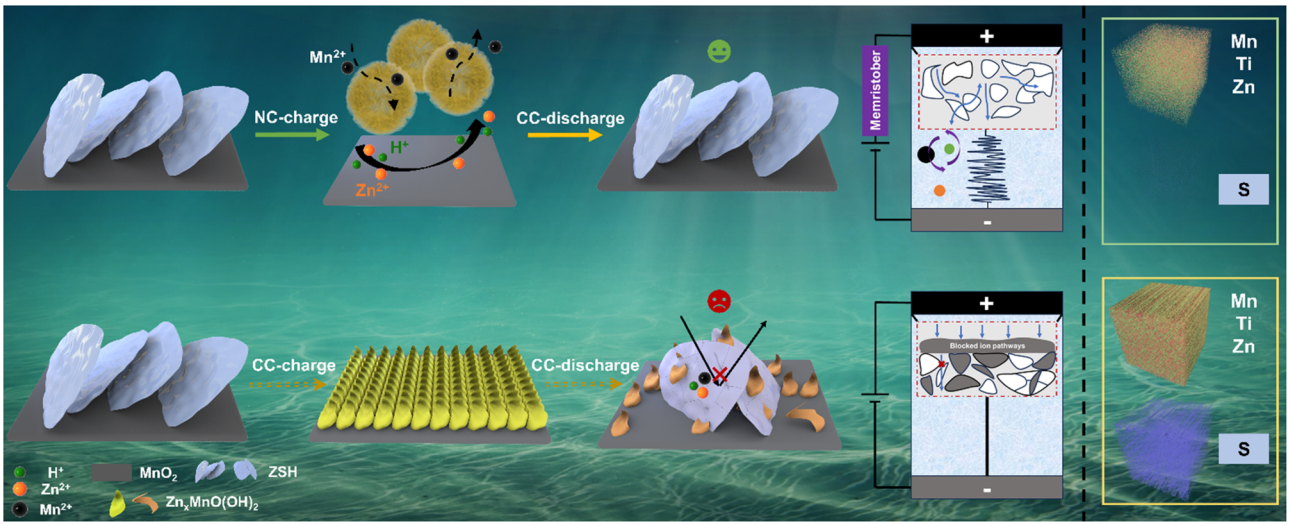

Fig. 4 Schematic illustration of the ZSH-to-ZMO conversion mechanism under chaotic current activation. TOF-SIMS analysis and corresponding 3D distribution of diverse fragments (150 nm) for chaos-activated and pristine electrodes after 500 cycles.

−13.46 for the original cathode. This improvement indicates enhanced ion transport pathways and faster charge-transfer kinetics, contributing to superior electrochemical dynamics. Furthermore, as shown in Fig. S13, CV analyses at different scan rates were performed to distinguish capacitive and diffusion-controlled contributions. The results indicate that the pseudocapacitive contribution increases with scan rate, ensuring fast responses at high current densities. More importantly, the activated cathode predominantly exhibits diffusion-controlled behavior, which facilitates the stable reversible transformation of ZSH/ZMO as well as the electrochemical processes of Zn^{2+} and H^{+}.

To further evaluate practical applicability, we fabricated a flexible battery with an area of 2 × 2 cm^2 and ∼8 mg active material loading. As shown in Fig. 3g and h, the chaos-activated flexible battery exhibits excellent diffusion behavior ($\log D = -12.27$) and outstanding rate performance, retaining 92.81 mAh g^{-1} after 1555 cycles at a high current density of 1000 mA g^{-1}, with a capacity retention of 76.9%. This result is superior to the battery activated under conventional constant current conditions. In addition, the performance with respect to the MnO_2 analogs reported in the literature is shown in Table S2. These findings clearly demonstrate that the nonlinear chaotic current enables synergistic regulation of structural evolution and interfacial reaction kinetics, significantly enhancing the electrochemical performance and durability.

In conventional Zn–Mn aqueous batteries, inactive byproducts such as ZSH and ZMO gradually accumulate on the electrode surface during cycling, thereby hindering interfacial reaction kinetics and restricting charge transport. This accumulation significantly impairs both capacity retention and cycling stability. As cycling progresses, the irreversible buildup of these byproducts intensifies, continuously reducing the effective reactive surface area and leading to rapid performance degradation. To address this challenge, a nonlinear chaotic circuit was introduced for pre-activation charging, enabling dynamic modulation of the electrode through non-periodic, strongly perturbative, and high-frequency transient stimulation. An optimized activation protocol involving seven cycles of chaotic current excitation was identified, which markedly promotes the reversible ZSH ↔ ZMO transformation. Unlike the conventional charge–discharge pathway, where ZSH and ZMO deposit with sluggish conversion dynamics, chaotic excitation introduces a more complex electric field distribution and dynamic current perturbation at the early stage. This facilitates the activation of multiple electron/ion transport pathways, thereby inducing the controllable formation and reversible transformation of ZSH and ZMO and ensuring high reversibility during the initial phase of structural evolution.

Moreover, by tuning the governing equations through the d value (defining chaotic fluctuation characteristics, Fig. S14 and S15) and the k_3 value (controlling amplitude, Fig. S16 and S17), chaotic yet controllable signals were generated, with the d value regulating the local distribution of the chaotic field and the k_3 value determining its amplitude. The V–A data confirm that the system consistently retains homogeneity and oscillatory dynamics within the operational range. The performance enhancement primarily stems from the chaotic field generated by the nonlinear circuit, which provides a persistent dynamic driving force and induces macroscopic chaotic current oscillations, thereby continuously disrupting and reorganizing ion-transport pathways. Compared with constant-voltage or single-waveform charging, this chaotic field—with its spatio-temporal non-uniformity and dynamic reconstruction—effectively suppresses ion accumulation and concentration polarization, reduces surface coverage by byproducts, and markedly improves the uniformity and accessibility of interfacial reactions. Consequently, the system achieves a synergistic optimization of reaction kinetics and structural stability during cycling, delivering performance gains beyond the reach of conventional charging modes.

From the perspective of interfacial regulation and reaction kinetics, chaotic current excitation suppresses the rapid accumulation of intermediate ZSH/ZMO phases through high-frequency dynamic perturbation, while significantly enhancing Zn^{2+} diffusion flux and charge transfer rates, thereby enabling their early involvement in reversible redox processes. Structurally, this pre-activation strategy promotes the formation of a uniform and stable reaction phase distribution, delays electrode degradation, and mitigates the continuous buildup of inactive byproducts. Under chaotic circuit activation, the fluctuating current induces dynamic ionic driving forces that not only unblock and interconnect ion-transport pathways but also facilitate rapid migration through the channels. Moreover, nonlinear perturbations promote reversible ion insertion and extraction within the electrode materials, thereby enabling synergistic enhancement of ion transport and conversion dynamics.

To validate this mechanism, time-of-flight secondary ion mass spectrometry (ToF-SIMS) was performed on electrodes after 500 cycles in the fully charged state at 1.9 V. Three-dimensional reconstruction was conducted to visualize the spatial distribution of elements.[55–57] The results reveal significant sulfur accumulation on the surface of untreated electrodes, which is closely associated with residual ZSH. This indicates continuous deposition of sulfur-containing byproducts during cycling.

Notably, based on the electrochemical conversion pathway, ZMO does not contain sulfur in its structure, confirming that the detected sulfur signal originates from residual ZSH or other sulfur-based side products. In contrast, electrodes subjected to chaotic pre-activation exhibited negligible sulfur signals, suggesting effective conversion of ZSH during charging. This provides further evidence that the chaotic excitation strategy successfully promotes the reversible transformation between ZSH and ZMO. Importantly, the ToF-SIMS mapping also shows that Zn, Ti, and Mn remain uniformly distributed throughout the electrode, indicating that chaotic current application does not compromise the intrinsic structural integrity of the material. These findings underscore the practical stability and long-term viability of the proposed activation strategy. They also confirm the mechanistic role of chaotic excitation from a spatial distribution perspective and provide direct insights into how nonlinear perturbation aids in regulating side-product conversion.

In situ XRD was employed to investigate the ion storage behavior of the cathode activated by chaotic current during the charging and discharging processes. The primary energy storage mechanisms, including the Zn^{2+}/H^{+} insertion/extraction process and the reversible conversion between ZMO and ZSH, were examined. Firstly, the *in situ* XRD data revealed

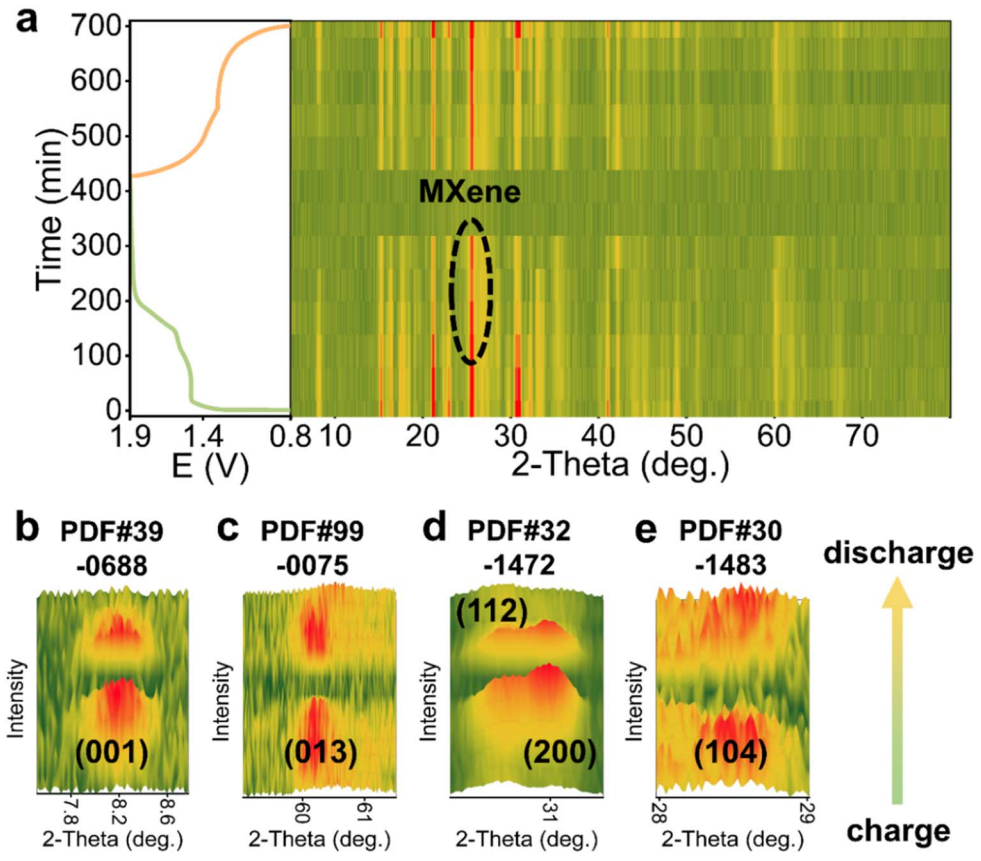

Fig. 5 (a) *In situ* XRD analysis contour plot of the cathode material during the charging and discharging process after activation by chaotic current. (b) The (001) peak of ZSH, (c) the (013) peak of MnOOH, (d) the (112) and (002) peaks of $Zn_2Mn_3O_8$, and (e) the (104) peak of $ZnMn_3O_7$ in selected 2θ ranges.

that the chaotic current-activated material structure retains the 2D heterostructure of a-MnO_2/Ti_3C_2F during cycling, ensuring efficient ion transport and mechanical stability (Fig. 5a).[52] Secondly, Fig. 5b and c show the periodic and symmetrical appearance and disappearance of the (001) diffraction peak of the ZSH phase and the (013) diffraction peak of MnOOH, with no significant peak shift, indicating that the insertion and extraction of Zn^{2+} and H^+ ions are highly reversible, while the material's lattice structure remains stable throughout this process.[20,22] Finally, the insertion of Zn^{2+} ions induced local changes in the lattice structure. As shown in Fig. 5d, when Zn^{2+} ions insert to form $Zn_2Mn_3O_8$, the (112) and (200) diffraction peaks exhibit reversible changes, with the (200) peak intensity surpassing the (112) peak during charging, suggesting that Zn^{2+} insertion causes local relaxation or rearrangement of the MnO_2 lattice. In Fig. 5e, the insertion of Zn^{2+} to form $ZnMn_3O_7$ results in reversible changes and a slight shift of the (104) diffraction peak, indicating that the insertion and extraction of Zn^{2+} ions induce minor changes in the lattice, possibly due to the interaction between Zn^{2+} ions and oxygen ions in the MnO_2 lattice, leading to local structural rearrangement or distortion.[21,41,42] Specifically, in combination with the *in situ* XRD results of the original electrode (Fig. S18), the results clearly demonstrate that, compared with the original electrode, the chaos-activated electrode exhibits more distinct ZSH peak evolution and more stable diffraction peak positions and intensities, revealing a more complete and highly reversible ZSH/ZMO transformation process. Therefore, chaotic current activation preserves the 2D heterostructure of the material while enabling the reversible conversion between ZMO and ZSH, ensuring efficient insertion and extraction of both Zn^{2+} and H^+ ions.

Thermogravimetric analysis (TGA) provides intrinsic insight into the thermal stability and energy release of cathodes. Such thermodynamic data are critical for assessing potential risks under extreme conditions and are particularly valuable for ensuring safety and reliability in large-scale energy storage applications. Therefore, the thermodynamic characteristics of the electrode materials after 500 cycles were further examined by TGA. A comprehensive description of the applied models and methodologies can be found in Section S3 of the SI. As demonstrated in Fig. 6a and b, the isoconversional method was employed to calculate and corroborate the thermodynamic parameters of the cathode materials. To evaluate the activation energy (E_a), several non-isothermal kinetic models were utilized, including the Friedman, Starink, Vyazovkin, Kissinger–Akahira–Sunose (KAS), and Flynn–Wall–Ozawa (FWO) models.[58–61] The corresponding E_a values and correlation coefficients (R^2) are summarized in Tables S3 and S4. As shown in Fig. 6b and S19, the results derived from these models reveal the relationships between the conversion rate α and heating rate β, as well as the variations of E_a and R^2 across different α values. All models consistently indicate that the cycled chaos-activated cathode exhibits superior overall thermodynamic behavior compared to the cycled pristine electrode, with a significantly higher average activation energy (NC cycled = 221.95 kJ mol^{-1} *vs.* CC cycled = 157.44 kJ mol^{-1}). As shown in Fig. 6c, all average R^2 values are above 0.95, confirming the high reliability of the calculated E_a values. Furthermore, strong agreement is observed among the E_a results obtained from different models, which underscores the consistency and accuracy of the data. Therefore, through the integrated analysis of multiple kinetic models, we reliably assessed the thermal stability of the cathode materials. The findings demonstrate that the activated electrode exhibits superior thermal safety performance compared to the original electrode.

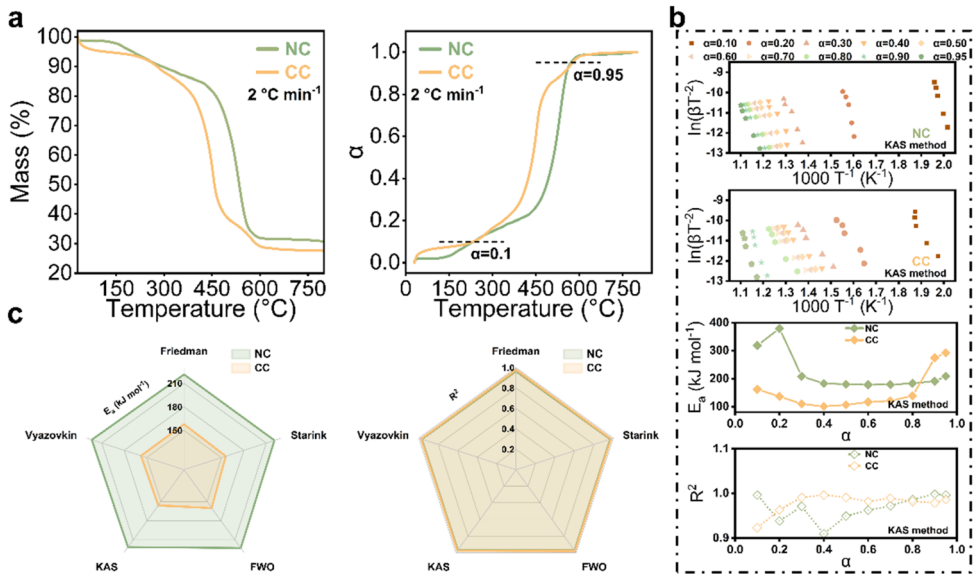

Fig. 6 (a) TG tests at β of 2, 4, 10, 15, and 20 °C min^{-1} for chaos-activated and pristine materials after 500 cycles, along with the corresponding α–temperature variation curves. (b) Thermokinetic model fitting using the KAS method based on TG data for chaos-activated and pristine materials after 500 cycles. (c) E_a and R^2 using the Friedman, KAS, Starink, Vyazovkin and FWO kinetic methods.

Conclusions

In summary, this study investigates the directional induction mechanism driving electrode structure reconstruction triggered by nonlinear current modes. The introduction of nonlinear current, particularly in chaotic regimes during charging, aligns more effectively with inherent electrochemical reaction kinetics. The disordered nature of chaotic currents facilitates reversible transformation between $Zn_4SO_4(OH)_6 \cdot nH_2O$ (ZSH) and $Zn_xMnO(OH)_2$ (ZMO), reducing the accumulation of electrochemically inactive phases at the surface and minimizing performance degradation. Nonlinear currents induce fractal reconstructions that optimize electron and ion transport/diffusion, thereby improving electrochemical and thermal stability. Electrochemical tests demonstrate that the activated Zn–Mn battery exhibits high reversible capacity, excellent rate capability, and robust cycling stability, with the flexible device retaining 76.37% of its initial capacity after 1550 cycles at a current density of 1 A g^{-1}. Thermal stability analysis confirms superior structural integrity in the activated cathode. This study establishes correlations between current dynamics and phase transformations, elucidates the activation mechanism underlying reversible ZSH/ZMO conversions under nonlinear conditions, and provides a novel framework for designing high-performance Zn–Mn batteries.

Author contributions

Yang Song: investigation, writing – original draft preparation, methodology, visualization. Haidong Zhong: methodology, supervision, writing – review & editing. Tingting Hu: investigation, methodology. Jun Du: writing – review & editing, project administration. Changyuan Tao: visualization, writing – review & editing, project administration. Qian Zhang: conceptualization, writing – review & editing, methodology.

Conflicts of interest

There are no conflicts to declare.

Data availability

The data that support the findings of this study are available from the corresponding author upon reasonable request.

Supplementary information: details on synthesis and materials characterization; the sequenced nonlinear-current strategy; electrochemical performance and ion-diffusion kinetics; ion insertion/extraction and the reversible conversion mechanism; and assessments of electrode stability. See DOI: **https://doi.org/10.1039/d5sc06137g**.

Acknowledgements

This work was supported by the National Natural Science Foundation of China (Grant No. 22403011), Natural Science Foundation of Chongqing (Grant No. CSTB2024NSCQ-MSX0810), Chongqing Oversea Student Innovation Plan (cx2024025), National Key Research and Development Program of China (Grant number 2023YFC3904401), and Guangxi Science and Technology Program (AB24010229).

Notes and references

1 G. Zhu, J. Zhu, W. Jiang, Z. Zhang, J. Wang, Y. Zhu and Q. Zhang, *Appl. Catal., B*, 2017, **209**, 729–737.
2 S. Park, I. Kristanto, G. Y. Jung, D. B. Ahn, K. Jeong, S. K. Kwak and S.-Y. Lee, *Chem. Sci.*, 2020, **11**, 11692–11698.
3 L. Meng, Y. Zhu, Y. Lu, T. Liang, L. Zhou, J. Fan, Y. C. Kuo, P. Guan, T. Wan, L. Hu and D. Chu, *ChemElectroChem*, 2023, **11**, e202300495.
4 S. Wei, Y. Wang, S. Chen and L. Song, *Chem. Sci.*, 2024, **15**, 7848–7869.
5 M. Lin, F. Shao, S. Weng, S. Xiong, S. Liu, S. Jiang, Y. Xu, Y. Jiao and J. Chen, *Electrochim. Acta*, 2021, **378**, 138147.
6 X. Zheng, K. Xu, Y. Ma, J. Sun, B. Han, R. Luo, M. Wang, N. Chen, L. Song, Q. Zhao and W. Chen, *Adv. Energy Mater.*, 2024, **14**, 2400038.
7 T. Jiang, D. Shen, Z. Zhang, H. Liu, G. Zhao, Y. Wang, S. Tan, R. Luo and W. Chen, *Nat. Rev. Clean Technol.*, 2025, **1**, 474–492.
8 W. Liu, X. Zhang, Y. Huang, B. Jiang, Z. Chang, C. Xu and F. Kang, *J. Energy Chem.*, 2021, **56**, 365–373.
9 J. Huang, X. Tang, K. Liu, G. Fang, Z. He and Z. Li, *Mater. Today Energy*, 2020, **17**, 100475.
10 M. Shi, B. Wang, C. Chen, J. Lang, C. Yan and X. Yan, *J. Mater. Chem. A*, 2020, **8**, 24635–24644.
11 Y. Huang, J. Mou, W. Liu, X. Wang, L. Dong, F. Kang and C. Xu, *Nano–Micro Lett.*, 2019, **11**, 49.
12 D. Zhao, X. Pu, S. Tang, M. Ding, Y. Zeng, Y. Cao and Z. Chen, *Chem. Sci.*, 2023, **14**, 8206–8213.
13 X. Li, Z. Xu, Y. Qian and Z. Hou, *Energy Storage Mater.*, 2022, **53**, 72–78.
14 G. Zhang, J. Zhu, L. Lin, Y. Liu, S. Li, Q. Li, X.-X. Liu and X. Sun, *Chem. Sci.*, 2024, **15**, 3545–3551.
15 K.-H. Ha, H. Moon, E. J. Joo, D. H. Jo and K. T. Lee, *Energy Storage Mater.*, 2024, **65**, 103150.
16 W. Liu, Q. Su, R. Zhu, W. Shi, F. Zhang, G. Du, W. Zhao, M. Zhang and B. Xu, *ACS Appl. Energy Mater.*, 2023, **6**, 6689–6699.
17 Z. Liu, Y. Yang, B. Lu, S. Liang, H. J. Fan and J. Zhou, *Energy Storage Mater.*, 2022, **52**, 104–110.
18 X. Pu, X. Li, L. Wang, H. Maleki Kheimeh Sari, J. Li, Y. Xi, H. Shan, J. Wang, W. Li, X. Liu, S. Wang, J. Zhang and Y. Wu, *ACS Appl. Energy Mater.*, 2022, **14**, 21159–21172.
19 S. Deng, B. Xu, J. Zhao, C. W. Kan and X. Liu, *Angew. Chem., Int. Ed.*, 2024, **63**, e202401996.
20 H. Chen, C. Dai, F. Xiao, Q. Yang, S. Cai, M. Xu, H. J. Fan and S. J. Bao, *Adv. Mater.*, 2022, **34**, 2109092.
21 N. Jiang, Y. Zeng, Q. Yang, P. Lu, K. Qu, L. Ye, X. Lu, Z. Liu, X. Li, Y. Tang, J. Cao, S. Chen, C. Zhi and J. Qiu, *Energy Environ. Sci.*, 2024, **17**, 8904–8914.
22 Z. Wang, Y. Fang, J. Shi, Z. Ma, X. Qu and P. Li, *Adv. Energy Mater.*, 2024, **14**, 2303739.

23 S. Jain, V. Novosad, F. Y. Fradin, J. E. Pearson, V. Tiberkevich, A. N. Slavin and S. D. Bader, *Nat. Commun.*, 2012, **3**, 1330.
24 A. V. Ievlev, S. Jesse, A. N. Morozovska, E. Strelcov, E. A. Eliseev, Y. V. Pershin, A. Kumar, V. Y. Shur and S. V. Kalinin, *Nat. Phys.*, 2013, **10**, 59–66.
25 Y. Li, C. Li, S. Zhang, G. Chen and Z. Zeng, *IEEE Trans. Ind. Electron.*, 2022, **69**, 10564–10572.
26 J. Yang, C. Li, Q. Zhang, X. Zhang, Z. Wu, H. Zhong, P. Liu, Z. Liu, C. Tao, K. Huang, J. Li and G. Zheng, *Chaos Solitons Fractals*, 2024, **183**, 114832.
27 R. M. Kent, W. A. S. Barbosa and D. J. Gauthier, *Nat. Commun.*, 2024, **15**, 3886.
28 J. Yang, C. Li, Q. Zhang, Z. Wu, P. Liu, Z. Liu, C. Tao, G. Zheng, Y. Yang and H. Wei, *Chem. Eng. J.*, 2025, **503**, 158195.
29 H. Li, Y. Yu, T. Wang, Y. Zhang, J. You, F. Hu and K. Zhu, *J. Power Sources*, 2024, **610**, 234638.
30 P. Eribol, S. K. Gopalakrishnan, S. V. Diwakar, A. Talbi, R. Narayanan, F. Zoueshtiagh and K. J. Ziegler, *Electrochim. Acta*, 2023, **462**, 142616.
31 X. Zeng, J. Liu, J. Mao, J. Hao, Z. Wang, S. Zhou, C. D. Ling and Z. Guo, *Adv. Energy Mater.*, 2020, **10**, 190163.
32 H. Mkaouar and O. Boubaker, *Commun. Nonlinear Sci. Numer. Simul.*, 2012, **17**, 1292–1302.
33 W. Fan, S. Tian, L. Qin, T. S. Alomar, P. Ruan, Z. M. El-Bahy, N. AlMasoud, B. Lu and J. Zhou, *J. Am. Chem. Soc.*, 2025, **147**, 18694–18703.
34 U. S. Thounaojam, *Chaos Solitons Fractals*, 2022, **165**, 112763.
35 Z. Xie, Z. Liu, J. Chang, Y. Qin and C. Tao, *ACS Sustain. Chem. Eng.*, 2020, **8**, 15044–15054.
36 Y.-f. Cui, Z.-b. Zhuang, Z.-l. Xie, R.-f. Cao, Q. Hao, N. Zhang, W.-q. Liu, Y.-h. Zhu and G. Huang, *ACS Nano*, 2022, **16**, 20730–20738.
37 J. Yang, C. Li, Q. Zhang, H. Zhong, Z. Wu, P. Liu, Z. Liu, K. Huang, C. Tao, G. Zheng, Y. Yang and H. Wei, *Chem. Eng. Sci.*, 2024, **293**, 120010.
38 Z. Yao, K. Sun and S. He, *Chaos Solitons Fractals*, 2024, **184**, 114970.
39 J. Zuo, J. Zhang, X. Wei, L. Yang, N. Cheng and J. Lv, *Chaos Solitons Fractals*, 2024, **187**, 115331.
40 C. Wu, L. Xiong and N. Yang, *Chaos Solitons Fractals*, 2024, **186**, 115222.
41 Y. Song, W. Zhan, Z. Wu, Q. Chen, X. Chen, Z. Liu, J. Du, C. Tao and Q. Zhang, *J. Mater. Chem. A*, 2024, **12**, 16910–16920.
42 Y. Zuo, T. Meng, H. Tian, L. Ling, H. Zhang, H. Zhang, X. Sun and S. Cai, *ACS Nano*, 2023, **17**, 5600–5608.
43 X. Li, C. Ji, J. Shen, J. Feng, H. Mi, Y. Xu, F. Guo and X. Yan, *Adv. Sci.*, 2023, **10**, 2205794.
44 Z. Liu, M. Han, S. Zhang, H. Li, X. Wu, Z. Fu, H. Zhang, G. Wang and Y. Zhang, *Adv. Mater.*, 2024, **36**, 2404188.
45 M. Zhu, R. Gao, Q. Ran, S. g. Gong, Q. Li, S. P. Zeng, H. Huang, L. Hu, D. Yang, T. Dai, Y. Wang, D. Chao, M. Feng and Z. Chen, *Angew. Chem., Int. Ed.*, 2025, **64**, e202425080.
46 Z. H. Sun, W. Zheng, R. Zheng, Z. Y. Gu, Y. Bao, Z. B. Liu, Z. B. Sun, L. Niu and X. L. Wu, *Adv. Sci.*, 2025, **12**, 2502745.
47 Z. Liu, H. Li, M. Han, L. Fang, Z. Fu, H. Zhang, G. Wang and Y. Zhang, *Adv. Energy Mater.*, 2023, **13**, 2302058.
48 W. Sun, F. Wang, S. Hou, C. Yang, X. Fan, Z. Ma, T. Gao, F. Han, R. Hu, M. Zhu, *et al.*, *J. Am. Chem. Soc.*, 2017, **139**, 9775–9778.
49 T. Li, N. Zhang, B. Liu, P. Wang, Z. Liu, Y. Wang, D. Xu, H. Tian, Q. Zhang and T. F. Yi, *Adv. Funct. Mater.*, 2025, **35**, 2423755.
50 X. Wang, W. Zhou, L. Wang, Y. Zhang, S. Li, X. Li, Z. Zhao, T. Zhang, H. Jin, X. Song, P. Liang, B. Zhang, D. Zhao and D. Chao, *Adv. Mater.*, 2025, **37**, 2501049.
51 S. Zhang, W. Zuo, X. Fu, J. Li, Q. Zhang, W. Yang, H. Chen, J. Zhang, X. Xiao, K. Amine, S.-G. Sun, F. Fu, M. Ye and G.-L. Xu, *Nat. Commun.*, 2025, **16**, 4052.
52 Q. Liang, S. Wang, X. Lu, X. Jia, J. Yang, F. Liang, Q. Xie, C. Yang, J. Qian, H. Song and R. Chen, *ACS Nano*, 2024, **18**, 2395–2408.
53 Y. Cheng, Y. Xie, S. Yan, Z. Liu, Y. Ma, Y. Yue, J. Wang, Y. Gao and L. Li, *Sci. Bull.*, 2022, **67**, 2216–2224.
54 M. Peng, L. Wang, L. Li, X. Tang, B. Huang, T. Hu, K. Yuan and Y. Chen, *Adv. Funct. Mater.*, 2021, **32**, 2109524.
55 H. Zhang, M. Zhang, R. Liu, T. He, L. Xiang, X. Wu, Z. Piao, Y. Jia, C. Zhang, H. Li, F. Xu, G. Zhou and Y. Mai, *Nat. Commun.*, 2024, **15**, 5451.
56 J. Li, S. Sun, H. Huang, T. Zhai, Y. Liu, M. Gu, H. Yang, M. Sun, T. Kou, S. Li and H. Xia, *J. Am. Chem. Soc.*, 2025, **147**, 6886–6896.
57 Y. Li, B. Wen, N. Li, Y. Zhao, Y. Chen, X. Yin, X. Da, Y. Ouyang, X. Li, P. Kong, S. Ding, K. Xi and G. Gao, *Angew. Chem., Int. Ed.*, 2024, **64**, e202414636.
58 Z. Wu, J. Yang, S. Qin, J. Li, Q. Zhang, J. Du, C. Tao, Q. Chen, L. Shi, C. Li and Z. Liu, *Chem. Eng. J.*, 2025, **503**, 158614.
59 Z.-H. Wu, Y. Wu, Y. Tang, J.-C. Jiang and A.-C. Huang, *Process Saf. Environ. Prot.*, 2023, **169**, 285–292.
60 C.-Z. Zhang, J.-C. Jiang, A.-C. Huang, Y. Tang, L.-J. Xie, J. Zhai and Z.-X. Xing, *Process Saf. Environ. Prot.*, 2022, **164**, 555–565.
61 Y.-C. Liu, J.-C. Jiang, A.-C. Huang, Y. Tang, Y.-P. Yang, H.-L. Zhou, J. Zhai, Z.-X. Xing, C.-F. Huang and C.-M. Shu, *Process Saf. Environ. Prot.*, 2022, **160**, 91–101.